Model of Raman scattering in self-assembled InAs/GaAs quantum dots

S. N. Klimin,* V. M. Fomin,† and J. T. Devreese‡
Theoretische Fysica van de Vaste Stoffen (TFVS), Universiteit Antwerpen, B-2020 Antwerpen, Belgium

D. Bimberg
Institut für Festkörperphysik, Technische Universität Berlin, PN 5-2, Hardenbergstrasse 36, D-10623 Berlin, Germany
(Received 20 July 2007; published 9 January 2008)

Multiphonon resonant Raman scattering in self-assembled quantum disks is investigated using a nonadiabatic approach. The optical phonons and the electron-phonon interaction are considered within the multimode dielectric continuum model. The model exploits both electrostatic and mechanical boundary conditions for the relative ionic displacement vector, as well as the phonon spatial dispersion in bulk. The confined phonon modes in a quantum dot are hybrids of bulklike and interface vibrations. It is shown that nonadiabatic effects substantially increase the Raman scattering probabilities and the relative multiphonon integral intensities with respect to the one-phonon intensity. The calculated ratio of the two- and one-phonon integral intensities is close to the experimental value for self-organized InAs/GaAs quantum dots.

DOI: 10.1103/PhysRevB.77.045307 PACS number(s): 78.66.−w, 61.46.−w, 63.22.−m, 78.30.−j

I. INTRODUCTION

Experiments on Raman scattering in self-assembled quantum dots[1–7] have revealed a rich structure of peaks caused by optical-phonon-assisted quantum transitions. The Raman spectra of disk-shaped GaAs/AlAs quantum dots, measured in Refs. 1 and 2, show the presence of phonon modes specific for quantum dots.[8] In Refs. 3–6, experimental evidence that specific phonon modes whose frequencies differ from those of LO and TO phonons exist in self-assembled InAs/GaAs quantum dots is presented. They are interpreted as interface phonons. Raman peaks assigned to interface phonons of self-assembled GaN/AlN quantum dots are observed in Ref. 9.

In Refs. 4–6, one- and two-phonon Raman bands are observed in self-assembled quantum dots. These results confirm the conclusion of Ref. 10 regarding the enhanced efficiency of the electron-phonon interaction in quantum dots. The dependence of this efficiency on the quantum-dot size is determined by several factors. First, when a finite-height potential barrier exists at the interface of a quantum dot, an increased separation of the electron and hole charges can arise due to their different masses. This enhances the efficiency of the exciton-phonon interaction. The second factor of such an enhancement in quantum dots is the effect of nonadiabaticity, first studied in Ref. 11 (see also, e.g., Refs. 12–14).

Various theoretical investigations led to different conclusions regarding the efficiency of the exciton-phonon interaction as a function of the quantum-dot size, depending on the chosen model. In Ref. 15, a donorlike exciton model for a spherical quantum dot was considered, where the hole was treated as a charge localized in the center of a quantum dot. It was found within this model that the Huang-Rhys parameter did not depend on the quantum-dot radius. Contrary to Ref. 15, for the same model, an increase of the exciton polaron effect with decreasing quantum-dot size was obtained using a variational method in Ref. 16. A nonmonotonous size dependence of the exciton-phonon interaction energy was obtained in Ref. 17: for decreasing dot radius, the LO-phonon contribution to the exciton energy decreased from the bulk value and then rapidly increased after reaching a minimum. The Raman cross section was studied for weak confinement of an exciton in a CuBr quantum dot in Ref. 18, where it was shown that the Huang-Rhys parameter increases with decreasing dot radius. The Raman measurements[19] showed that the so-called experimental Huang-Rhys factor, as determined from the intensities of the observed Raman peaks, rises with decreasing size of the quantum dot. Also the experimental data of Refs. 20 and 21 indicate that the effective strength of the carrier-phonon coupling is larger in smaller quantum nanostructures. The theoretical conclusions of Refs. 10–14, 16, and 18 are in line with experiment.

The effects of the nonadiabaticity of the exciton-phonon system in spherical CdSe and PbS quantum dots in the strong-confinement regime were shown in Refs. 11–13 to lead to a significant rise of the probabilities of phonon-assisted transitions and to a considerable distinction of the Raman and photoluminescence spectra from the Franck-Condon progression. The enhancement of the exciton-phonon interaction makes possible the experimental observation of multiphonon Raman scattering in quantum dots, as confirmed by recent measurements of two-phonon Raman bands in self-organized InAs/GaAs quantum dots.[4,5] The nonadiabatic effects bring a key contribution also to the optical absorption, photoluminescence, and photoluminescence excitation of self-assembled quantum dots.[5,14,22–24]

In the present work, we investigate multiphonon resonant Raman scattering via exciton transitions in disk-shaped quantum dots, which constitute a model for self-assembled quantum dots. Within our model, we assume in-plane parabolic confinement and a finite rectangular interface-barrier confinement in the axial direction. This model allows us to calculate the exciton states in a quantum dot by a variational method for a wide range of the in-plane confinement frequency parameter from the weak-confinement regime to the

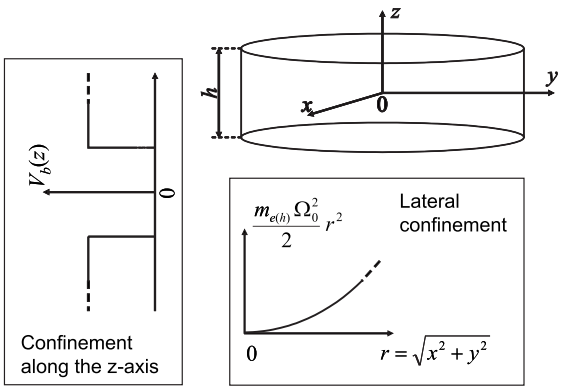

FIG. 1. Schematic picture of a disk-shaped quantum dot.

strong-confinement regime. Using the formalism of Refs. 11 and 13, we take into account the effects of nonadiabaticity, which play a crucial role in the optical spectra of quantum dots.

The paper is organized as follows. In Sec. II, we describe the excitons and optical phonons in disk-shaped quantum dots and represent our nonadiabatic approach to the multiphonon Raman scattering. The numerical results of that approach for the disk-shaped quantum dots are discussed in Sec. III, which is followed by the conclusions, Sec. IV.

II. EXCITONS, OPTICAL PHONONS, AND RAMAN SCATTERING IN QUANTUM DOTS

A. Excitons

We consider a disk-shaped quantum dot of height h $(-h/2<z<h/2)$, see Fig. 1. The in-plane confinement for the electrons and holes is ensured by a parabolic potential with frequency parameter Ω_0. The medium inside (outside) the quantum dot is indicated by the index 1 (2).

The exciton-phonon Hamiltonian of the system under consideration has the form

$$\hat{H} = \hat{H}_{ex}(\mathbf{r}_e, \mathbf{r}_h) + \sum_{\nu} \hbar\omega_{\nu}\hat{a}_{\nu}^{\dagger}\hat{a}_{\nu} + \sum_{\nu} (\beta_{\nu}\hat{a}_{\nu} + \beta_{\nu}^{*}\hat{a}_{\nu}^{\dagger}), \quad (1)$$

where H_{ex} $(\mathbf{r}_e, \mathbf{r}_h)$ is the exciton Hamiltonian, and r_e and r_h are the coordinates of the electron and hole, respectively. $\beta_{\nu}=\gamma_{\nu}(\mathbf{r}_e)-\gamma_{\nu}(\mathbf{r}_h)$ is the exciton-phonon interaction amplitude for the νth phonon mode with frequency ω_{ν} and carrier-phonon interaction amplitude $\gamma_{\nu}(\mathbf{r})$, and $\hat{a}_{\nu}^{\dagger}$ $(\hat{a}_{\nu})$ are the phonon creation (annihilation) operators. The exciton Hamiltonian in the effective-mass approach is

$$\begin{aligned}\hat{H}_{ex}(\mathbf{r}_e, \mathbf{r}_h) = &-\frac{\hbar^2}{2}\frac{\partial}{\partial z_e}\left(\frac{1}{m_e(z)}\frac{\partial}{\partial z_e}\right) - \frac{\hbar^2}{2}\frac{\partial}{\partial z_h}\left(\frac{1}{m_h(z)}\frac{\partial}{\partial z_h}\right) \\ &- \frac{\hbar^2}{2m_e(z)}\left(\frac{\partial^2}{\partial x_e^2} + \frac{\partial^2}{\partial y_e^2}\right) - \frac{\hbar^2}{2m_h(z)}\left(\frac{\partial^2}{\partial x_h^2} + \frac{\partial^2}{\partial y_h^2}\right) \\ &+ U_c(\mathbf{r}_e, \mathbf{r}_h) + \frac{m_e(z_e)\Omega_0^2}{2}\mathbf{r}_{e\|}^2 + \frac{m_h(z_h)\Omega_0^2}{2}\mathbf{r}_{h\|}^2 \\ &+ V_e(z_e) + V_h(z_h). \quad (2)\end{aligned}$$

The notation $m_{e(h)}(z)$ means that we take into account the distinction between electron (hole) effective masses in the quantum dot (medium 1) and those in the host substance (medium 2):

$$m_{e(h)}(z) = \begin{cases} m_{1,e(h)}, & |z| < h/2 \\ m_{2,e(h)}, & |z| \geqslant h/2. \end{cases} \quad (3)$$

In Eq. (2), U_c $(\mathbf{r}_e, \mathbf{r}_h)$ is the Coulomb electron-hole interaction potential, and $V_{e(h)}(z)$ is the interface-barrier potential:

$$V_{e(h)}(z) = \begin{cases} 0, & |z| < h/2 \\ V_{e(h)}^{b}, & |z| \geqslant h/2. \end{cases} \quad (4)$$

In the present work, we consider the case where the height of the quantum dot is much smaller than both the exciton Bohr radius and the effective in-plane radius of the quantum dot, $R_0=\sqrt{\hbar/(2\mu_1\Omega_0)}$, where μ_1 is the reduced mass of the electron and hole in the quantum dot. Eigenstates of the exciton Hamiltonian in Eq. (2), which are used for the calculation of the Raman spectra, are approximated using a variational method, assuming a strong-confinement regime along the z axis. We choose the variational wave functions in the form

$$\Psi_{N_eN_h,n_1m_1,n_2m_2}(\mathbf{r}_e, \mathbf{r}_h) = \phi_{N_e}^{e}(z_e)\phi_{N_h}^{h}(z_h)\Psi_{n_1m_1,n_2m_2}^{(\|)}(\boldsymbol{\rho}_e, \boldsymbol{\rho}_h), \quad (5)$$

where the axial wave functions $\phi_{N_{e(h)}}^{e(h)}(z)$ are the eigenfunctions of the Hamiltonian of the electron (hole) motion along the z axis:

$$\hat{H}_{e(h)}^{\perp}(z) \equiv -\frac{\hbar^2}{2}\frac{\partial}{\partial z}\left(\frac{1}{m_{e(h)}(z)}\frac{\partial}{\partial z}\right) + V_{e(h)}(z), \quad (6)$$

with the following current-conserving boundary conditions at the interface:[25]

$$\begin{cases} \phi_{N_{e(h)}}^{e(h)}\left[\pm\left(\dfrac{h}{2}-\delta\right)\right] = \phi_{N_{e(h)}}^{e(h)}\left[\pm\left(\dfrac{h}{2}+\delta\right)\right], \\ \dfrac{1}{m_{e(h)}(z)}\dfrac{\partial}{\partial z}\phi_{N_{e(h)}}^{e(h)}(z)\Big|_{z=\pm(h/2-\delta)} = \dfrac{1}{m_{e(h)}(z)}\dfrac{\partial}{\partial z}\phi_{N_{e(h)}}^{e(h)}(z)\Big|_{z=\pm(h/2+\delta)} \end{cases} \quad (\delta \to +0). \quad (7)$$

The in-plane motion of the exciton is described by the wave functions

$$\Psi^{(\|)}_{n_1m_1,n_2m_2}(\boldsymbol{\rho}_e,\boldsymbol{\rho}_h)=\Phi_{n_1m_1}(R)\frac{1}{\sqrt{2\pi}}e^{im_1\varphi_1}\psi_{n_2m_2}(\rho)\frac{1}{\sqrt{2\pi}}e^{im_2\varphi_2}, \tag{8}$$

which depend on the coordinate vectors $\boldsymbol{\rho}_e,\boldsymbol{\rho}_h$. The functions $\Phi_{n_1m_1}(R)\frac{1}{\sqrt{2\pi}}e^{im_1\varphi_1}$ and $\psi_{n_2m_2}(\rho)\frac{1}{\sqrt{2\pi}}e^{im_2\varphi_2}$ describe, respectively, the quantum states of the in-plane center-of-mass motion and the relative motion of the electron and hole. m_1 and m_2 are the quantum numbers of the angular momentum, and n_1 and n_2 are "radial" quantum numbers. The details of the mathematical procedure used to obtain the excitonic wave functions $\Phi_{n_1m_1}(R)$ and $\psi_{n_2m_2}(\rho)$ are described in the Appendix.

B. Optical phonons

Within the present investigation, the optical phonons in the quantum dot are calculated using the multimode dielectric continuum model.[13,26,27] In the case where the sizes of the quantum dot substantially exceed the lattice constant a_0, the optical phonons in both the quantum dot and the host medium are described by the relative ionic displacement vector $\mathbf{u}(\mathbf{r})=\mathbf{u}_+(\mathbf{r})-\mathbf{u}_-(\mathbf{r})$, where $\mathbf{u}_\pm(\mathbf{r})$ are displacements of the positive and negative ions, respectively. The dynamics of the dispersive optical phonons in the long-wavelength region is determined by the generalized Born-Huang equation.[13] This equation takes the following form in the Fourier representation with respect to time:

$$(\omega_{\mathrm{TO}}^2-\omega^2)\mathbf{u}=\omega_{\mathrm{TO}}\left(\frac{\varepsilon_0-\varepsilon_\infty}{4\pi\rho_0}\right)^{1/2}\mathbf{E}+\int\mathbb{T}(\mathbf{r}-\mathbf{x})\mathbf{u}(\mathbf{x},\omega)d\mathbf{x}, \tag{9}$$

where ρ_0 is the reduced ionic mass density, $\mathbf{E}$ is the macroscopic electric field, ω_{TO} is the bulk TO-phonon frequency at the Brillouin zone center, and ε_∞ and ε_0 are the high-frequency and static dielectric constants, respectively. The spatial dispersion tensor $\mathbb{T}(\mathbf{r}-\mathbf{x})$ describes the short-range forces which provide the LO and TO bulk phonon dispersions.

The eigenfrequencies and the basis vectors of the phonon modes are found by the joint solution of Eq. (9) together with the static Maxwell equation for the displacement $\mathbf{D}=\varepsilon_\infty\mathbf{E}+\omega_{\mathrm{TO}}\sqrt{4\pi(\varepsilon_0-\varepsilon_\infty)\rho_0}\mathbf{u}$,

$$\mathrm{div}\,\mathbf{D}=0. \tag{10}$$

For the quantum dot under consideration, Eqs. (9) and (10) should be obeyed for each medium separately. The solution of this set of equations is subjected to boundary conditions. Those are subdivided into electrostatic [for $\mathbf{E}(\mathbf{r})$ and $\mathbf{D}(\mathbf{r})$] and mechanical [for $\mathbf{u}(\mathbf{r})$] boundary conditions. The mechanical boundary conditions are chosen from the following considerations. First, for structures for which the frequencies of the optical phonons in adjacent media substantially differ from each other, optical vibrations cannot propagate from one medium to another. Second, the electrostatic interaction between lattice cells is modeled by the interaction between dipoles, which is strongly anisotropic. Taking into account this anisotropy, the following boundary conditions[28] are applicable:

$$u_\perp|_{\mathrm{boundary}}=0,\qquad \partial\mathbf{u}_\|/\partial\xi_n|_{\mathrm{boundary}}=0, \tag{11}$$

where the subscripts $\perp$ and $\|$ denote, respectively, the normal and tangential (with respect to the boundary) components of a vector, and ξ_n is the coordinate along the axis directed normal to the boundary. As pointed out in Refs. 28 and 29, the distinction between the boundary conditions in Eq. (11) and the "rigid" boundary conditions, in which $\mathbf{u}|_{\mathrm{boundary}}=0$, leads to only a marginal difference in the resulting phonon mode frequencies.

Equations (9) and (10) are solved by substituting $\mathbf{u}(\mathbf{r})$ as a sum over basis vectors, which satisfy the boundary conditions in Eq. (11). As distinct from the dielectric continuum model (DCM) (see, e.g., Refs. 30 and 31), we find that LO-phonon modes, in general, are not bulklike or interface but have a hybrid character.

From Eqs. (9) and (10) with Eq. (11), dispersion equations are derived for the eigenfrequencies of phonon modes of even (s) and odd (a) parities, whose electrostatic potentials are, respectively, symmetric and antisymmetric with respect to the inversion of the z axis:

$$\varepsilon_{1s}(q_\|,\omega)\tanh\left(\frac{\zeta}{2}\right)+\varepsilon_2(\omega)=0\quad\text{for even modes},$$

$$\varepsilon_{1a}(q_\|,\omega)\coth\left(\frac{\zeta}{2}\right)+\varepsilon_2(\omega)=0\quad\text{for odd modes}, \tag{12}$$

where $\zeta=q_\|h$, $q_\|$ is the modulus of the in-plane phonon wave vector $\mathbf{q}_\|$, and $\varepsilon_2(\omega)$ is the dielectric function of the host medium. The functions $\varepsilon_{1s(a)}(q_\|,\omega)$ take the form

$$\varepsilon_{1j}(q_\|,\omega)=\varepsilon_1(\infty)\left[1-\sum_{n=0}^{n_{\max}}\chi_{j,n}(q_\|)\frac{\omega_{1,\mathrm{LO}}^2(0)-\omega_{1,\mathrm{TO}}^2(0)}{\omega_{1,\mathrm{LO}}^2(Q_{j,n})-\omega^2}\right]^{-1}, \tag{13}$$

with the dispersive optical-phonon frequencies $\omega_{1,\mathrm{LO}}(Q)$ and $\omega_{1,\mathrm{TO}}(Q)$. The phonon wave number Q can have the discrete values

$$Q_{j,n}=\begin{cases}\sqrt{q_\|^2+\left(\frac{2n\pi}{h}\right)^2}, & j=s\\ \sqrt{q_\|^2+\left[\frac{(2n+1)\pi}{h}\right]^2}, & j=a.\end{cases} \tag{14}$$

The coefficients $\chi_{j,n}(q_\|)$ are determined by

$$\chi_{s,n}(q_\|)=\frac{2(2-\delta_{n,0})q_\|}{hQ_{s,n}^2}\tanh\left(\frac{\zeta}{2}\right),\quad \chi_{a,n}(q_\|)=\frac{4q_\|}{hQ_{a,n}^2}\coth\left(\frac{\zeta}{2}\right). \tag{15}$$

The summation over n in Eq. (13) is limited by the value $n_{\max}=[h/(2a_0)]$. This limitation expresses the fact that the wavelength of an optical phonon cannot be smaller than

twice the lattice constant a_0. Therefore, the present approach explicitly takes into account the finite number of the phonon modes in a quantum dot.

As distinct from the approach of Refs. 29 and 32, Ref. 13 allows us to take into account the nonquadratic dispersion of the optical phonons. The approach of Refs. 29 and 32 has been later extended to a nonquadratic phonon dispersion[33,34] simulated by an analytical spherically symmetric expression. The method of Ref. 13, however, leads to the dispersion equation [Eq. (12)] with the effective dielectric function [Eq. (13)], which is valid for a more general dispersion law, $\omega_{j,\mathrm{LO(TO)}}(Q)$, for the optical phonons in bulk than that used in Refs. 33 and 34. In particular, in Eq. (13), one can use numerical data for the bulk optical-phonon frequencies in order to calculate the optical-phonon spectra for quantum dots.

Using the formal analogy of the dispersion equations in Eq. (12) with those for the interface phonon modes of DCM,[31] we can interpret $\varepsilon_{1j}(q_\parallel,\omega)$ as the effective dielectric function of the quantum dot. As distinct from the dielectric function for bulk, there exists a set of dielectric functions for a quantum dot, which describe the polarization response due to even ($j=s$) and odd ($j=a$) optical-phonon modes, respectively. It is worth noting that the functions $\varepsilon_{1j}(q_\parallel,\omega)$ are dispersive, since they depend on both ω and the modulus of the in-plane wave vector $\mathbf{q}_\parallel$.

The calculation of the frequencies of the hybrid phonon modes in the InAs/GaAs quantum dots has been performed using the parameters of the bulk optical phonons of InAs and GaAs from Refs. 35 and 36. The frequencies of several phonon modes of an InAs/GaAs disk-shaped quantum dot with parameters $h=8$ nm and $\hbar\Omega_0=20$ meV are shown as a function of $q_\parallel$ in Fig. 2. The hybrid InAs modes of the quantum dot can have frequencies within the reststrahlen band of bulk InAs. It appears that an even hybrid mode exists with a frequency close to the TO-phonon frequency of InAs. This mode is formed mainly by the interface vibrations and is referred to as an interfacelike mode. It has a larger dispersion as compared to other hybrid InAs modes and results in a Raman peak of considerable relative intensity. For the odd InAs phonon modes, strong mixing exists between the bulklike and interface phonons. For the GaAs phonons, the multimode dielectric continuum approach provides half-space modes and interfacelike modes with frequencies close to those obtained within DCM.

The size dependence of the optical-phonon frequencies in InAs/GaAs disk-shaped quantum dots for a definite value of the in-plane wave vector $q_\parallel$ is represented in Fig. 3. In order to explicitly show mixing between bulklike and interface InAs modes, we also plot the interface optical-phonon frequencies obtained within DCM in Fig. 3. The anticrossings of the bulklike and interface phonon frequencies are clearly seen for even modes [Fig. 3(a)]. In the consecutive intervals of the quantum-dot height, the frequency of one of hybrid InAs mode (interfacelike) becomes close to the frequency of the interface InAs mode from DCM. For example, the first even hybrid InAs mode is interfacelike in the range $h \lesssim 2$ nm. The second even InAs mode is interfacelike for 2.5 nm$\lesssim h \lesssim$4 nm.

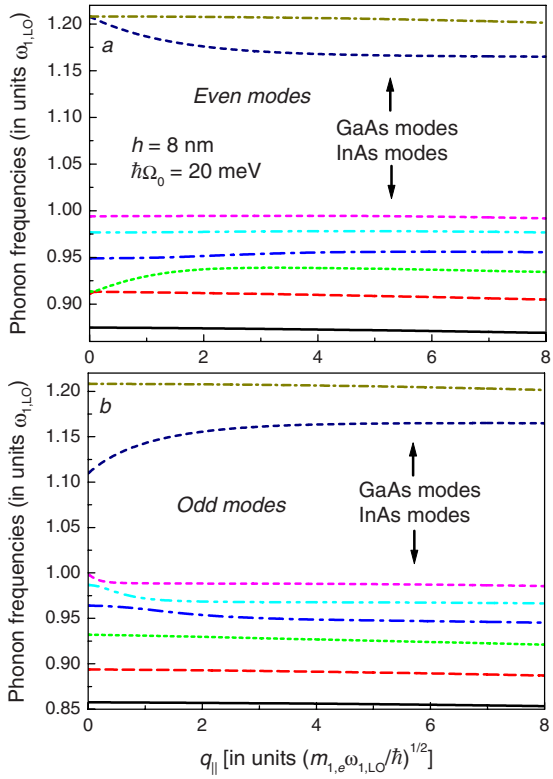

FIG. 2. (Color online) Frequencies of the (a) even and (b) odd hybrid phonon modes in an InAs/GaAs disk-shaped quantum dot with the parameters $h=8$ nm and $\hbar\Omega_0=20$ meV as a function of the modulus of the in-plane wave vector $\mathbf{q}_\parallel$. The dotted curves in panel (a) in the frequency ranges $0.9\omega_{1,\mathrm{LO}} \lessapprox \omega \lessapprox 0.95\omega_{1,\mathrm{LO}}$ and $1.15\omega_{1,\mathrm{LO}} \lessapprox \omega \lessapprox 1.21\omega_{1,\mathrm{LO}}$ correspond, respectively, to the even interfacelike InAs and GaAs modes, which have a considerable dispersion. For the odd modes, a strong coupling of the bulklike and interface phonons occurs in the frequency range $0.95\omega_{1,\mathrm{LO}} \lessapprox \omega \lessapprox 0.98\omega_{1,\mathrm{LO}}$. The interfacelike odd GaAs phonon mode lies in the frequency range $1.11\omega_{1,\mathrm{LO}} \lessapprox \omega \lessapprox 1.15\omega_{1,\mathrm{LO}}$. Frequencies of other hybrid modes in the figure are close to those for the bulklike phonons and possess a relatively weak dispersion.

C. Multiphonon Raman intensities

Within the framework of the long-wavelength approximation, the interaction of an electron with an electromagnetic field is described by the operator $\hat{V}(t)=\hat{V}_I e^{-i\Omega_I t}+\hat{V}_S^\dagger e^{i\Omega_S t}$, where the terms with $\hat{V}_I$ and $\hat{V}_S^\dagger$ correspond, respectively, to the absorption of a photon with frequency Ω_I (incoming light) and to the emission of a photon with frequency Ω_S (scattered light). The interaction amplitude $\hat{V}_{I(S)}$ is proportional to the projection of the electron dipole moment operator $\hat{\mathbf{d}}$ on the polarization vector $\mathbf{e}^{I(S)}$ of the relevant wave: $\hat{d}^{I(S)}=\mathbf{e}^{I(S)}\cdot\hat{\mathbf{d}}$. In Refs. 12 and 13, the expression for the Raman scattering probability has been derived using an exact averaging in the general expression for the Raman cross section[37] over the phonon states.

In general, the account of nonadiabaticity requires nonperturbative approaches (see, e.g., Refs. 24 and 38). However, for quantum dots, in which the electron-phonon cou-

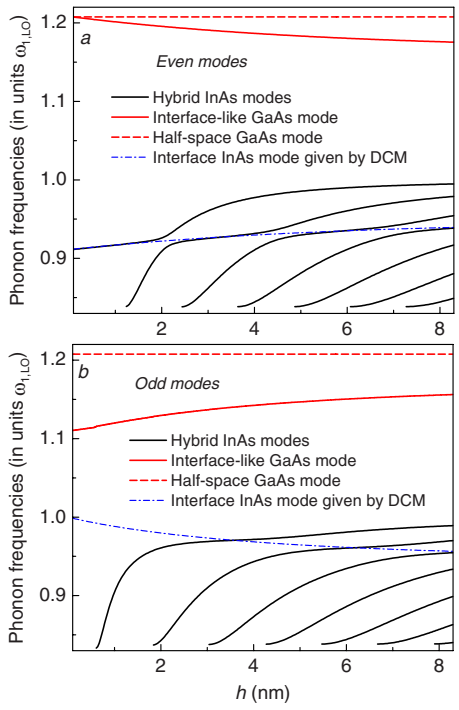

FIG. 3. (Color online) Frequencies of the (a) even and (b) odd hybrid phonon modes in an InAs/GaAs disk-shaped quantum dot as a function of the quantum-dot height at the modulus of the in-plane wave vector $q_{\parallel}=2$ [in units $(m_{1,e}\omega_{1,\mathrm{LO}}/\hbar)^{1/2}$]. Solid black curves are hybrid InAs phonon modes. Solid and dashed red curves are interfacelike and half-space GaAs modes, respectively. Dot-dashed blue curves are interface InAs modes given by DCM.

pling constant is small ($\alpha=0.052$ in InAs and $\alpha=0.068$ in GaAs), the leading-term expansion is an adequate approximation in order to interpret the observed Raman peak intensities. It was first applied to the Raman scattering in quantum dots in Ref. 12. Within this expansion, the K-phonon scattering intensity, corresponding to a definite combinatorial frequency $\Sigma_{j=1}^{K}\omega_{\nu_j}$, can be analyzed to lowest (Kth) order in the electron-phonon coupling constant. The scattering intensity is then expressed through a squared modulus of the scattering amplitude,[12,13]

$$F_K^{(\pm)}(\nu_1,\ldots,\nu_K)=\sum_{\mu_0\cdots\mu_K}\frac{(d_{\mu_0}^I)^* d_{\mu_K}^S}{\tilde{\omega}_{\mu_0}-\Omega_I+i\tilde{\Gamma}_{\mu_0}}\times\prod_{j=1}^{K}\frac{\langle\mu_j|\beta_{\nu_j}|\mu_{j-1}\rangle}{\tilde{\omega}_{\mu_j}-\Omega_I\pm\sum_{k=1}^{j}(\omega_{\nu_k}\pm i\Gamma_{\nu_k})+i\tilde{\Gamma}_{\mu_j}}. \tag{16}$$

Here, $\tilde{\omega}_{\mu}$ is the frequency and $d_{\mu}^{I(S)}\equiv\langle 0|\hat{d}^{I(S)}|\mu\rangle$ is the dipole matrix element of a transition between the exciton vacuum and the eigenstate $|\mu\rangle$ of the Hamiltonian $\hat{H}_{ex}$, as given by Eq. (5), $\tilde{\Gamma}_{\mu}$ is the inverse lifetime of an exciton in the state $|\mu\rangle$, and Γ_{ν} is the inverse lifetime for the νth phonon mode. In Ref. 39, a formula equivalent to Eq. (16), except for the phonon inverse lifetimes, was obtained by a systematic perturbation expansion of the scattering amplitude.

D. Selection rules

1. Dipole matrix elements

The matrix elements for the exciton optical transitions[40] are proportional to the envelope integrals

$$d_{\mu}^{I(S)}\propto\int d\mathbf{r}_e\int d\mathbf{r}_h\Psi_{N_eN_h,n_1m_1,n_2m_2}(\mathbf{r}_e,\mathbf{r}_h)\delta(\mathbf{r}_e-\mathbf{r}_h)$$
$$=\frac{1}{2\pi}\psi_{n_2m_2}(0)\int_{-\infty}^{\infty}dz\phi_{N_e}^{e}(z)\phi_{N_h}^{h}(z)\times\int_0^{\infty}RdR\int_0^{2\pi}d\varphi\Phi_{n_1m_1}(R)e^{im_1\varphi}. \tag{17}$$

The wave function $\psi_{n_2m_2}(0)$ is other than zero for $m_2=0$. The integral over R is other than zero for $m_1=0$. So, we find that

$$d_{\mu}^{I(S)}\propto\delta_{m_1,0}\delta_{m_2,0}\psi_{n_2,0}(0)\int_{-\infty}^{\infty}\phi_{N_e}^{e}(z)\phi_{N_h}^{h}(z)dz\int_0^{\infty}\Phi_{n_1,0}(R)RdR. \tag{18}$$

Herefrom, for the exciton angular moments in the initial (μ_0) and final (μ_K) states for the center-of-mass motion, the selection rules follow

$$m_1(0)=0,\quad m_1(K)=0, \tag{19}$$

and for the relative motion,

$$m_2(0)=0,\quad m_2(K)=0. \tag{20}$$

The integral over z in Eq. (18) is other than zero only when the wave functions $\phi_{N_e}^{e}(z)$ and $\phi_{N_h}^{h}(z)$ are of the same parity (both even or both odd).

2. Exciton-phonon matrix elements

The amplitude of the exciton-phonon interaction is the difference of the amplitudes of the electron-phonon and hole-phonon interactions,

$$\beta_{\nu}(\mathbf{r}_e,\mathbf{r}_h)=\gamma_{\nu}(\mathbf{r}_e)-\gamma_{\nu}(\mathbf{r}_h), \tag{21}$$

where r_e and r_h are the coordinates of an electron and a hole, respectively. The electron-phonon interaction amplitude can be represented in the form

$$\gamma_{\nu}(\mathbf{r})\equiv\gamma_{k,\mathbf{q}_{\parallel}}(z,\boldsymbol{\rho})=\tilde{\gamma}_{k,q_{\parallel}}(z)e^{i\mathbf{q}_{\parallel}\cdot\boldsymbol{\rho}}. \tag{22}$$

The index k labels the phonon modes of the same modulus $q_{\parallel}$ of the in-plane wave vector. The amplitudes $\tilde{\gamma}_{k,q_{\parallel}}(z)$ possess a definite parity with respect to the inversion in the z direction, i.e., they are even or odd, according to the symmetry of the electrostatic potentials of phonon modes.

As follows from Eqs. (5), (21), and (22), the matrix elements of the exciton-phonon interaction amplitudes are

$$\langle \mu|\beta_\nu|\mu'\rangle = \delta_{N_h,N_h'}\langle \phi^e_{N_e}|\tilde{\gamma}_{k,q_\parallel}|\phi^e_{N_e'}\rangle\langle \Psi^{(\parallel)}_{n_1m_1,n_2m_2}|e^{i\mathbf{q}_\parallel\cdot\boldsymbol{\rho}_e}|\Psi^{(\parallel)}_{n_1'm_1',n_2'm_2'}\rangle - \delta_{N_e,N_e'}\langle \phi^h_{N_h}|\tilde{\gamma}_{k,q_\parallel}|\phi^h_{N_h'}\rangle\langle \Psi^{(\parallel)}_{n_1m_1,n_2m_2}|e^{i\mathbf{q}_\parallel\cdot\boldsymbol{\rho}_h}|\Psi^{(\parallel)}_{n_1'm_1',n_2'm_2'}\rangle. \quad (23)$$

Let us introduce the parity factor for exciton states, $P_{ex}=(-1)^{\zeta_e+\zeta_h}$, where $\zeta_{e(h)}=0$ and $\zeta_{e(h)}=1$, respectively, for the symmetric and antisymmetric electron (hole) axial wave functions. For even phonon modes, the matrix element $\langle \phi^{e(h)}_N|\tilde{\gamma}_{k,q_\parallel}|\phi^{e(h)}_{N'}\rangle$ is other than zero when $\phi^{e(h)}_N$ and $\phi^{e(h)}_{N'}$ have the same parity. For odd phonon modes, that matrix element is other than zero when $\phi^{e(h)}_N$ and $\phi^{e(h)}_{N'}$ have different parities. Therefore, the emission of an odd-parity phonon changes the exciton state in such a way that the sign of P_{ex} is changed, and the emission of a phonon of even parity keeps P_{ex} unchanged. As follows from the above selection rules for dipole matrix elements, for both initial and final exciton states, $P_{ex}=1$. As a result, the multiphonon Raman scattering processes with only an even number of odd phonon modes are allowed. In particular, the odd phonon modes do not contribute to the one-phonon Raman scattering amplitude.

III. RESULTS AND DISCUSSION

In Fig. 4, we have plotted one- and two-phonon Raman spectra for disk-shaped InAs/GaAs quantum dots with different values of the dot height h and of the in-plane confinement frequency Ω_0. In order to analyze the role of nonadiabaticity, Raman spectra have been calculated by two methods: (i) within the nonadiabatic approach, where transitions through all intermediate states are taken into account, and (ii) in the adiabatic approximation (see Ref. 15), when nondiagonal matrix elements of the exciton-phonon interaction are neglected. The results of nonadiabatic and adiabatic approaches are shown in Fig. 4 as solid and dashed lines, respectively.

The material parameters of the semiconductors are taken from Ref. 35. The LO- and TO-phonon energies at the Brillouin zone center are $\hbar\omega_{1,\mathrm{LO}}=30.03$ meV, $\hbar\omega_{1,\mathrm{TO}}=27.36$ meV, $\hbar\omega_{2,\mathrm{LO}}=36.25$ meV, and $\hbar\omega_{2,\mathrm{TO}}=33.29$ meV. Raman intensities are plotted as a function of the Stokes energy shift $\Delta E\equiv\hbar(\Omega_I-\Omega_S)$. In Figs. 4(a) and 4(b), values of the parameters that are relevant for the experiment[4,5] are chosen: $h=8$ nm and $\hbar\Omega_0=20$ meV, which correspond to a radius $R_0=9.35$ nm. In Figs. 4(c)–4(f), we show Raman spectra for a quantum dot with a stronger confinement: $h=5$ nm and $\hbar\Omega_0=30$ meV ($R_0=7.64$ nm), and $h=4$ nm and $\hbar\Omega_0=50$ meV ($R_0=5.92$ nm).

The Raman spectra are averaged using the size distribution of quantum dots. For self-assembled quantum-dot structures, the exciton and phonon inverse lifetimes are typically small with respect to the inhomogeneous broadening. In this case, the Raman spectra of quantum dots do not depend on the exciton lifetimes. The size dispersion then enters a factor common for all Raman peaks. Because of the finite phonon lifetime, the Raman lines turn into broadened peaks, which

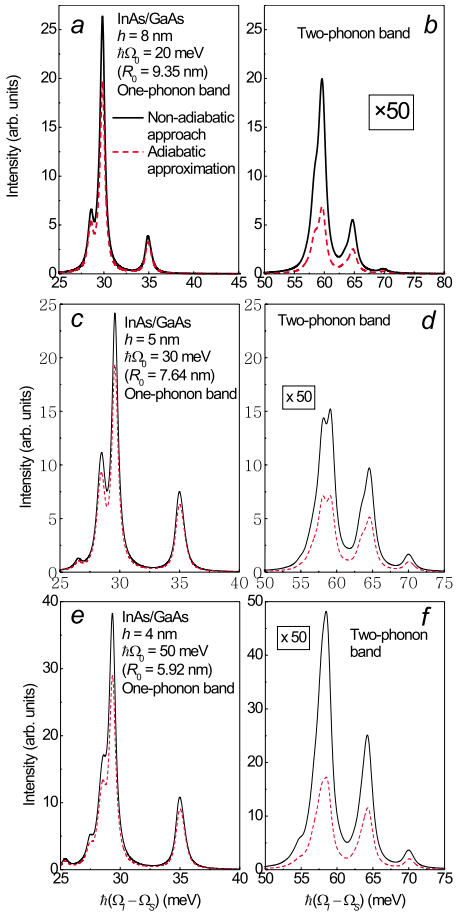

FIG. 4. (Color online) [(a), (c), and (e)] One-phonon and [(b), (d), and (f)] two-phonon Raman spectra for disk-shaped InAs/GaAs quantum dots with different values of the height and of the in-plane confinement frequency parameter. Solid curves show results obtained taking into account effects of nonadiabaticity. Dashed curves show results of the adiabatic approximation. The units for the Raman intensity are the same in all panels.

are modeled with Lorentzians. The broadening for one-phonon (two-phonon) Raman peaks constitutes Γ_ν ($2\Gamma_\nu$). We assign the value $\Gamma_\nu=0.01\omega_{1,\mathrm{LO}}$ to the inverse phonon lifetime in order to distinguish Raman peaks due to different phonon modes in Fig. 4.

In the one-phonon spectra, we can clearly distinguish two groups of peaks, whose frequencies lie in the regions of the optical-phonon frequencies of InAs and GaAs, respectively. Consequently, these peaks can be assigned to the InAs and GaAs phonon modes. The structure of the InAs group of peaks reflects the spectrum of the hybrid phonon modes. The hybridization of the GaAs phonons appears to be negligibly small (as distinct from the InAs phonons), so that they can be subdivided into half-space and interface GaAs phonons. The interaction of an exciton with the half-space GaAs phonons is relatively weak because it is determined only by the "tails" of the electron and hole wave functions outside the quantum dot.

The two-phonon Raman band consists of peaks related to different combinatorial (double InAs, double GaAs, and mixed InAs/GaAs) optical-phonon frequencies. We see from

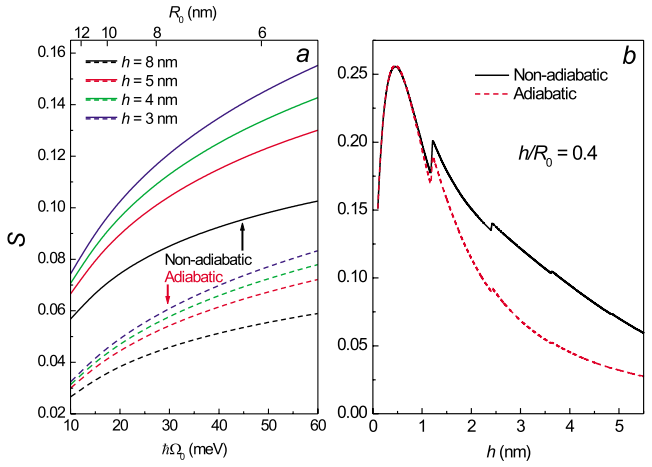

FIG. 5. (Color online) (a) The parameter S determined as $S \equiv 2I_2/I_1$, where I_1 and I_2 are the integral intensities of the one-phonon and the two-phonon Raman bands, respectively, as a function of the confinement energy $\hbar\Omega_0$. In the adiabatic approximation, S is the Huang-Rhys parameter. The solid curves are obtained taking into account nonadiabatic effects. The dashed curves correspond to the adiabatic approximation. (b) The parameter S as a function of the quantum-dot height of the disk-shaped InAs/GaAs quantum dot with h/R_0=0.4.

Fig. 4 that the effects of nonadiabaticity considerably enhance both the absolute values of the Raman peak intensities and the relative intensities of the two-phonon peaks with respect to those of the one-phonon peaks. This enhancement is provided by the larger number of quantum transitions for the nonadiabatic exciton-phonon coupling with respect to that for the adiabatic coupling in self-assembled InAs/GaAs quantum dots.

Comparing the calculated Raman spectra for different quantum-dot sizes with each other, we see that with strengthening confinement, a substantial increase of the scattering intensities occurs, especially for two-phonon scattering. This result suggests that the experimental observation of multiphonon Raman bands is facilitated in smaller self-assembled quantum dots.

In Fig. 5(a), we have plotted the parameter $S \equiv 2I_2/I_1$ (where I_1 and I_2 are the integral intensities of the one-phonon and two-phonon Raman bands, respectively) as a function of the in-plane confinement frequency for different values of the height of the quantum dot. The parameter S is a measure of the efficiency of the exciton-phonon interaction in the quantum dot. Within the adiabatic approximation, S coincides with the Huang-Rhys parameter,

$$S_{(\mathrm{A})} = \sum_{\nu} \frac{|\langle \mu_0 | \beta_\nu | \mu_0 \rangle|^2}{(\hbar\omega_\nu)^2}, \tag{24}$$

where $|\mu_0\rangle$ is the ground state of an exciton in the quantum dot. S increases with increasing confinement within the experimentally relevant range of the quantum-dot sizes.

In Fig. 5(b), the parameters S, both adiabatic and nonadiabatic, are plotted as a function of the quantum-dot height h keeping the aspect ratio constant. The variation of the number of phonon modes in the quantum dot is manifested through kinks of S as a function of h. The range of quantum-dot heights in the figure includes, in particular, extremely small values, $h \lesssim 1$ nm, which are not relevant for realistic self-assembled quantum dots but are considered here in order to investigate the small-size limit of the efficiency of the exciton-phonon interaction. As shown in Ref. 41, within the adiabatic approximation and with an infinite barrier, the Huang-Rhys parameter tends to zero in the limit of a quantum-dot size much smaller than the bulk exciton radius due to the local charge neutrality. In the present treatment, taking into account both nonadiabaticity and the finite barrier height, the dependence $S(h)$ is nonmonotonous owing to the following factors. On the one hand, a different penetration of the electron and hole wave functions into the barrier breaks the local charge neutrality. This factor leads to an increase of the efficiency of the exciton-phonon interaction with decreasing the height of the quantum dot. On the other hand, with decreasing the quantum-dot height, the spatial extent for both electron and hole wave functions outside the quantum dot increases. As a result, for extremely small quantum dots ($h \lesssim 1$ nm), S decreases with decreasing size. As seen from Fig. 5(b), in the range of experimentally relevant quantum-dot sizes, the nonadiabatic contribution dominates.

The ratio of the nonadiabatic to adiabatic parameters $S_{(\mathrm{NA})}/S_{(\mathrm{A})}$ in Fig. 5 decreases for increasing confinement frequency. This can be explained by the increasing energy difference between the various quantum levels of an exciton with increasing Ω_0, which lowers the relative probabilities of nonadiabatic transitions.

The influence of the nonadiabatic transitions on Raman spectra can be manifested through the breakdown of the Franck-Condon rule for scattering intensities. This breakdown can be revealed as follows. Within the adiabatic approximation, each (νth) phonon mode is characterized by its "oscillator strength,"

$$S_{\nu(\mathrm{A})} \equiv \frac{|\langle \mu_0 | \hat{\beta}_\nu | \mu_0 \rangle|^2}{(\hbar\omega_\nu)^2} \tag{25}$$

(which is referred to as the Huang-Rhys factor for a given phonon mode in Refs. 4 and 5). The sum of the oscillator strengths for all phonon modes is the total Huang-Rhys factor. The K-phonon scattering intensity $I_K(\nu_1, \ldots, \nu_K)$ of a peak, corresponding to a definite combinatorial frequency $\omega = \Sigma_{j=1}^{K} \omega_{\nu_j}$, is proportional to $\Pi_{j=1}^{K} S_{\nu_j(\mathrm{A})}$. In particular, the ratio

$$\frac{I_{2(\mathrm{A})}(\nu,\nu)}{[I_{1(\mathrm{A})}(\nu)]^2} = \mathrm{const}, \tag{26}$$

i.e., within the adiabatic approximation, this ratio is one and the same for all phonon modes, so that for any pair of different phonon modes, we have the relation

$$\frac{I_{2(\mathrm{A})}(\nu_1,\nu_1)}{I_{2(\mathrm{A})}(\nu_2,\nu_2)} = \left[\frac{I_{1(\mathrm{A})}(\nu_1)}{I_{1(\mathrm{A})}(\nu_2)}\right]^2. \tag{27}$$

When we take into account nonadiabatic effects, the rule in Eq. (27) breaks down.

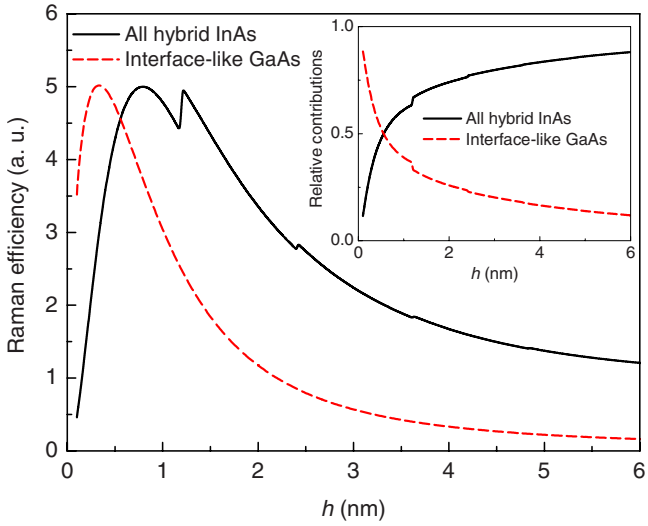

FIG. 6. (Color online) Absolute and (inset) relative contributions of all hybrid InAs and the interfacelike GaAs phonon modes into the one-phonon Raman scattering spectra as a function of the height of the disk-shaped InAs/GaAs quantum dot with $h/R_0=0.4$.

We conclude from estimations of the oscillator strengths of phonon modes made in Refs. 4 and 5, that the rule Eq. (27) is not fulfilled for the experiment.[4,5] Indeed, the interface phonon mode, which provides the most intensive one-phonon peak (at $\Delta E=35.9$ meV), appears to have the smallest oscillator strength: $S_{\mathrm{IF}}=0.006$. Therefore, the adiabatic approximation fails, and the effects of nonadiabaticity play a crucial role in the Raman spectra of the self-assembled InAs/GaAs quantum dots studied in Refs. 4 and 5.

The relative contribution of the interface modes to the calculated Raman spectra appears to be smaller than the corresponding contribution for the experimental Raman spectra of the self-assembled quantum dots. The contribution of those modes can considerably increase when taking into account, e.g., the composition inhomogeneity and the strain.

In Fig. 6, we analyze the absolute and relative contributions of all hybrid InAs and the interfacelike GaAs phonon modes into the one-phonon Raman intensity as a function of the size of the quantum dot keeping the aspect ratio constant. The contribution to the Raman intensity due to the half-space GaAs phonons appears to be relatively small within the considered range of the quantum-dot sizes. The contribution to the Raman intensity due to the interfacelike GaAs phonons reveals a pronounced size dependence. With decreasing the quantum-dot height, the relative contribution of the interfacelike GaAs phonons to the Raman intensity increases.

The spectral lines obtained in the Raman measurements, in general, may be provided not only by the Raman scattering but also by the phonon-assisted resonant luminescence. In Refs. 4 and 5, it was indicated that the resonant Raman scattering and luminescence under resonant excitation can be described as a unified second-order process.[42,43] In this connection, the distinction between resonant Raman scattering and resonant photoluminescence might become meaningless. Also, other channels can give a contribution to the measured resonant Raman spectra, for example, the nonresonant photoluminescence due to a secondary emission of quantum dots resonantly excited within inhomogeneously broadened high-energy exciton transitions (see, e.g., Refs. 44 and 45).

The resonant Raman spectra in Refs. 4 and 5 are obtained for excitation in the maximum of the ground-state photoluminescence, which corresponds to the maximum E_0 of the photoluminescence band at nonresonant excitation in Fig. 1(a) of Ref. 4. The width of that band is determined by the size dispersion of quantum dots. The statistic weight of quantum dots, in which the dipole optical transitions occur to the first excited state rather than to the ground state, can be estimated from the comparison of the intensity of the nonresonant photoluminescence, $I_{PL}(E_0-\Delta E)$, to $I_{PL}(E_0)$, where $\Delta E\sim 20$ meV is the typical difference between the ground and the first excited level of the exciton in the quantum dot. As seen from Fig. 1(a) of Ref. 4, $I_{PL}(E_0-\Delta E)$ is at least 1 order lower than $I_{PL}(E_0)$. This allows us to suppose that in the experiment of Refs. 4 and 5, the statistic weight of quantum dots, in which the optical transitions occur to excited states, is relatively low. The parameter $S\approx 0.075$ calculated for the experimentally relevant sizes $R_0\approx 9.35$ nm ($\hbar\Omega_0=20$ meV) and $h=8$ nm within the nonadiabatic approach is close to the value $S\approx 0.08$ obtained using the numerical integration of the experimental Raman spectra of Refs. 4 and 5. This closeness provides a support to our assumption that the calculated Raman spectra adequately interpret the experimental data of Refs. 4 and 5.

IV. CONCLUSIONS

We have calculated multiphonon Raman spectra in disk-shaped quantum dots which provide a model for self-assembled quantum dots. We take into account nonadiabatic effects[11,13] and specific optical-phonon modes, which are considered within the multimode dielectric continuum model.[13,26,27]

The relative contributions of different phonon modes into the Raman spectra depend both on the quantum-dot size and on the aspect ratio of the quantum dot. The relative contribution of the interfacelike GaAs phonons to the Raman spectra increases for increasing confinement strength.

With strengthening confinement within the experimentally relevant range of the quantum-dot sizes, the efficiency of the exciton-phonon interaction rises. The nonadiabatic transitions can substantially enhance the efficiency of the exciton-phonon interaction in quantum dots with respect to that calculated within the adiabatic approximation. When comparing different factors which contribute to the Raman intensity to each other, we can conclude that in the small-size limit, an increasing efficiency of the exciton-phonon interaction with a decreasing quantum-dot size is provided by the charge separation because of a finite barrier at the quantum-dot surface. However, in the experimentally relevant range of the quantum-dot sizes, the dominating contribution to the efficiency of the exciton-phonon interaction is due to nonadiabaticity.

ACKNOWLEDGMENTS

We are grateful to the late R. Heitz for providing the

experimental data. Discussions with V. N. Gladilin are acknowledged. One of us (D.B.) appreciates SFB 787 of DFG (Germany) for support of his work. This work has been supported by the FWO-Vl. Project No. G.0449.04, the WOG WO.035.04N (Belgium), and the European Commission SANDiE Network of Excellence, Contract No. NMP4-CT-2004-500101.

APPENDIX: WAVE FUNCTIONS FOR THE IN-PLANE MOTION OF AN EXCITON

The Hamiltonian for the in-plane motion of the exciton is obtained by averaging the exciton Hamiltonian with the ground-state wave functions,

$$H^{(\|)} \equiv \langle \phi_0^e | \langle \phi_0^h | H | \phi_0^h \rangle | \phi_0^e \rangle - \varepsilon_0^{(e,\perp)} - \varepsilon_0^{(h,\perp)}, \tag{A1}$$

where $\varepsilon_0^{(e,\perp)}$ and $\varepsilon_0^{(h,\perp)}$ are the contributions to the exciton ground-state energy due to the electron and hole motion along the z axis. The difference of the effective masses inside and outside the quantum dot is taken into account using the approximate Hamiltonian determined as follows:[46]

$$H^{(\|)} = \frac{\mathbf{p}_{e\|}^2}{2m_e} + \frac{\mathbf{p}_{h\|}^2}{2m_h} + \frac{m_e\Omega_0^2}{2}\boldsymbol{\rho}_e^2 + \frac{m_h\Omega_0^2}{2}\boldsymbol{\rho}_h^2 + U(\boldsymbol{\rho}_e - \boldsymbol{\rho}_h), \tag{A2}$$

with the masses

$$m_e \equiv 2m_{e1}\int_0^{l/2} |\phi_0^e(z)|^2 dz + 2m_{e2}\int_{l/2}^{\infty} |\phi_0^e(z)|^2 dz, \tag{A3}$$

$$m_h \equiv 2m_{h1}\int_0^{l/2} |\phi_0^h(z)|^2 dz + 2m_{h2}\int_{l/2}^{\infty} |\phi_0^h(z)|^2 dz, \tag{A4}$$

and the in-plane electron-hole interaction potential

$$U(|\boldsymbol{\rho}_e - \boldsymbol{\rho}_h|) = -\int_{-\infty}^{\infty} dz_e \int_{-\infty}^{\infty} dz_h \frac{e^2}{\varepsilon_\infty |\mathbf{r}_e - \mathbf{r}_h|} |\phi_0^e(z_e)\phi_0^h(z_h)|^2. \tag{A5}$$

Further, we introduce the coordinates of the center-of-mass and relative motions,

$$\mathbf{R} = \frac{m_e\boldsymbol{\rho}_e + m_h\boldsymbol{\rho}_h}{m_e + m_h}, \quad \boldsymbol{\rho} = \boldsymbol{\rho}_e - \boldsymbol{\rho}_h. \tag{A6}$$

In these coordinates, the Hamiltonian $H^{(\|)}$ is expressed as

$$H^{(\|)} = \frac{\mathbf{P}_\|^2}{2M} + \frac{\mathbf{p}_\|^2}{2\mu} + \frac{M\Omega_0^2}{2}\mathbf{R}^2 + \frac{\mu\Omega_0^2}{2}\rho^2 + U(\rho)$$

$$\left(M \equiv m_e + m_h, \quad \mu = \frac{m_e m_h}{m_e + m_h}\right) \tag{A7}$$

In the polar coordinates $R=(R,\varphi_1)$, $\rho=(\rho,\varphi_2)$, the wave functions of the in-plane motion are given by

$$\Psi^{(\|)}_{n_1m_1,n_2m_2} = \Phi_{n_1m_1}(R)\frac{1}{\sqrt{2\pi}}e^{im_1\varphi_1}\psi_{n_2m_2}(\rho)\frac{1}{\sqrt{2\pi}}e^{im_2\varphi_2}. \tag{A8}$$

Here, $\Phi_{nm}(R)$ is the radial eigenfunction of a two-dimensional oscillator with mass M and with frequency Ω_0. The energy levels of this subsystem are

$$\varepsilon_n^{(R)} = \hbar\Omega_0(n+1), \quad n = 0,1,\ldots .$$

The Hamiltonian of the relative in-plane motion is

$$H_\rho = -\frac{\hbar^2}{2\mu}\left(\frac{d^2}{d\rho^2} + \frac{1}{\rho}\frac{d}{d\rho} - \frac{m^2}{\rho^2}\right) + \frac{\mu\Omega_0^2}{2}\rho^2 + U(\rho).$$

In order to obtain a set of approximate eigenfunctions for the Hamiltonian in Eq. (A2), we use the Bogolubov inequality[47] for the ground-state energy,

$$E_\rho^0 \leqslant E_{\rho,0}^0 + \langle H_\rho - H_{\rho,0}\rangle_0, \tag{A9}$$

where $H_{\rho,0}$ is a model Hamiltonian for the in-plane relative motion.

We consider the case of a strong confinement, when the in-plane radius of the quantum dot is smaller than the effective Bohr radius of InAs, $a^*_{B,\mathrm{InAs}} \approx 29.8$ nm, which is in accordance with the experimental conditions of Refs. 4 and 5. In this case, the Coulomb attraction is expected to lead to a relatively small variation of the exciton transition energies and wave functions. By this reason, we can apply the Hamiltonian

$$H_{\rho,0} = -\frac{\hbar^2}{2\mu^*}\left(\frac{d^2}{d\rho^2} + \frac{1}{\rho}\frac{d}{d\rho} - \frac{m^2}{\rho^2}\right) + \frac{\mu^*(\Omega_0^*)^2}{2}\rho^2, \tag{A10}$$

with the variational parameters μ^* and Ω_0^*. After minimizing the variational functional in the right hand side of Eq. (A9), exact eigenfunctions of $H_{\rho,0}$ are used as an approximation for $\psi_{nm}(\rho)$.

TABLE I. Optimal values for the reduced exciton mass and for the confinement frequency for the relative in-plane motion of an exciton in the disk-shaped quantum dot with $h=5$ nm.

$\hbar\Omega_0$, meV	μ^*/μ	Ω_0^*/Ω_0
10	1.075	1.721
15	1.110	1.441
20	1.133	1.301
25	1.149	1.216
30	1.159	1.160

The optimal values for μ^* and Ω_0^* at several values of the in-plane confinement frequency and for $h=5$ nm are given in Table I. The Coulomb attraction results in an increase of the reduced exciton mass and of the in-plane confinement frequency for the relative motion of an electron and a hole. With strengthening confinement, the relative change of the reduced mass slightly increases, and the relative change of the confinement frequency decreases.

*Permanent address: Physics of Multilayer Structures, Department of Theoretical Physics, State University of Moldova, A. Mateevici 60, MD-2009 Chişinău, Moldova.

†Also at Photonics and Semiconductor Nanophysics, COBRA, Eindhoven University of Technology, P.O. Box 513, 5600 MB Eindhoven, The Netherlands; permanent address: Physics of Multilayer Structures, Department of Theoretical Physics, State University of Moldova, A. Mateevici 60, MD-2009 Chişinău, Moldova.

‡Also at Photonics and Semiconductor Nanophysics, COBRA, Eindhoven University of Technology, P.O. Box 513, 5600 MB Eindhoven, The Netherlands.

[1] P. Hawrylak, M. Potemski, D. J. Lockwood, H. J. Labbé, H. Kamada, H. Weman, J. Temmyo, and T. Tamamura, Physica E (Amsterdam) **2**, 652 (1998).

[2] C. M. Sotomayor Torres, D. J. Lockwood, and P. D. Wang, J. Electron. Mater. **29**, 576 (2000).

[3] A. G. Milekhin, A. I. Toropov, A. K. Bakarov, D. A. Tenne, G. Zanelatto, J. C. Galzerani, S. Schulze, and D. R. T. Zahn, Phys. Rev. B **70**, 085314 (2004).

[4] R. Heitz, H. Born, A. Hoffmann, D. Bimberg, I. Mukhametzhanov, and A. Madhukar, Appl. Phys. Lett. **77**, 3746 (2000).

[5] R. Heitz, A. Schliwa, and D. Bimberg, Phys. Status Solidi B **237**, 308 (2003).

[6] A. Milekhin, A. Toropov, A. Bakarov, S. Schulze, and D. Zahn, Phys. Status Solidi C **3**, 3924 (2006).

[7] W. J. Choi, H. Rho, J. D. Song, J. I. Lee, and Y. H. Cho, Physica E (Amsterdam) **26**, 115 (2005).

[8] S. N. Klimin, V. M. Fomin, J. T. Devreese, and J.-P. Leburton, in *Proceedings of the 200th Meeting of The Electrochemical Society and the 52nd Meeting of The International Society of Electrochemistry, San Francisco, CA, 2001* (The Electrochemical Society, New York, 2001), pp. 307–320.

[9] N. Garro, A. Cros, J. M. Llorens, A. García-Cristóbal, A. Cantarero, N. Gogneau, E. Sarigiannidou, E. Monroy, and B. Daudin, Phys. Rev. B **74**, 075305 (2006).

[10] V. M. Fomin, V. N. Gladilin, S. N. Klimin, J. T. Devreese, P. M. Koenraad, and J. H. Wolter, Phys. Rev. B **61**, R2436 (2000).

[11] V. M. Fomin, V. N. Gladilin, J. T. Devreese, E. P. Pokatilov, S. N. Balaban, and S. N. Klimin, Phys. Rev. B **57**, 2415 (1998).

[12] V. M. Fomin, E. P. Pokatilov, J. T. Devreese, S. N. Klimin, V. N. Gladilin, and S. N. Balaban, Solid-State Electron. **42**, 1309 (1998).

[13] E. P. Pokatilov, S. N. Klimin, V. M. Fomin, J. T. Devreese, and F. W. Wise, Phys. Rev. B **65**, 075316 (2002).

[14] V. N. Gladilin, S. N. Klimin, V. M. Fomin, and J. T. Devreese, Phys. Rev. B **69**, 155325 (2004).

[15] M. C. Klein, F. Hache, D. Ricard, and C. Flytzanis, Phys. Rev. B **42**, 11123 (1990).

[16] J. C. Marini, B. Stebe, and E. Kartheuser, Phys. Rev. B **50**, 14302 (1994).

[17] K. Oshiro, K. Akai, and M. Matsuura, Phys. Rev. B **66**, 153308 (2002).

[18] A. V. Fedorov, A. V. Baranov, and K. Inoue, Phys. Rev. B **56**, 7491 (1997).

[19] G. Scamarcio, V. Spagnolo, G. Ventruti, M. Lugará, and G. C. Righini, Phys. Rev. B **53**, R10489 (1996).

[20] R. P. Wang, G. Xu, and P. Jin, Phys. Rev. B **69**, 113303 (2004).

[21] L. Turyanska, A. Patanè, M. Henini, B. Hennequin, and N. R. Thomas, Appl. Phys. Lett. **90**, 101913 (2007).

[22] R. Heitz, S. Rodt, A. Schliwa, and D. Bimberg, Phys. Status Solidi B **238**, 273 (2003).

[23] T. A. Nguyen, S. Mackowski, H. E. Jackson, L. M. Smith, J. Wrobel, K. Fronc, G. Karczewski, J. Kossut, M. Dobrowolska, J. K. Furdyna, and W. Heiss, Phys. Rev. B **70**, 125306 (2004).

[24] M. I. Vasilevskiy and R. P. Miranda, Phys. Status Solidi C **2**, 862 (2005).

[25] T. Ando and S. Mori, Surf. Sci. **113**, 124 (1982).

[26] S. N. Klimin, E. P. Pokatilov, and V. M. Fomin, Phys. Status Solidi B **190**, 441 (1995).

[27] V. M. Fomin, S. N. Klimin, V. N. Gladilin, and J. T. Devreese, J. Lumin. **87-89**, 330 (2000).

[28] N. C. Constantinou and B. K. Ridley, Phys. Rev. B **49**, 17065 (1994).

[29] M. P. Chamberlain, M. Cardona, and B. K. Ridley, Phys. Rev. B **48**, 14356 (1993).

[30] R. Lassnig, Phys. Rev. B **30**, 7132 (1984).

[31] N. Mori and T. Ando, Phys. Rev. B **40**, 6175 (1989).

[32] E. Roca, C. Trallero-Giner, and M. Cardona, Phys. Rev. B **49**, 13704 (1994).

[33] M. I. Vasilevskiy, Phys. Rev. B **66**, 195326 (2002).

[34] A. G. Rolo and M. I. Vasilevskiy, J. Raman Spectrosc. **38**, 618 (2007).

[35] *Semiconductors. Physics of II—VI and I—VII Compounds, Semimagnetic Semiconductors*, Landolt-Börnstein, New Series, Group III, Vol. 17, Pt. b, edited by K. H. Hellwege (Springer, Berlin, 1982).

[36] S. Adachi, J. Appl. Phys. **58**, R1 (1985).

[37] M. Cardona, in *Light Scattering in Solids II*, Topics in Applied Physics Vol. 50, edited by M. Cardona and G. Güntherodt (Springer-Verlag, Heidelberg, 1982).

[38] R. P. Miranda, M. I. Vasilevskiy, and C. Trallero-Giner, Phys. Rev. B **74**, 115317 (2006).

[39] R. Rodríguez-Suárez, E. Menéndez-Proupin, C. Trallero-Giner, and M. Cardona, Phys. Rev. B **62**, 11006 (2000).

[40] R. J. Elliott, Phys. Rev. **108**, 1384 (1957).

[41] S. Schmitt-Rink, D. A. B. Miller, and D. S. Chemla, Phys. Rev. B **35**, 8113 (1987).

[42] Y. Toyozawa, J. Phys. Soc. Jpn. **41**, 400 (1976).

[43] Y. Toyozawa, A. Kotani, and A. Sumi, J. Phys. Soc. Jpn. **42**,

1495 (1977).
[44] R. Heitz, M. Veit, N. N. Ledentsov, A. Hoffmann, D. Bimberg, V. M. Ustinov, P. S. Kop'ev, and Zh. I. Alferov, Phys. Rev. B **56**, 10435 (1997).
[45] A. V. Baranov, V. Davydov, H.-W. Ren, S. Sugou, and Y. Masumoto, J. Lumin. **87-89**, 503 (2000).
[46] G. Hai, F. M. Peeters, and J. T. Devreese, Phys. Rev. B **42**, 11063 (1990).
[47] N. N. Bogolubov, J. Phys. (USSR) **11**, 23 (1947).